ELSEVIER

Journal of Atmospheric and Solar-Terrestrial Physics 69 (2007) 2465–2484

Journal of ATMOSPHERIC AND SOLAR-TERRESTRIAL PHYSICS

www.elsevier.com/locate/jastp

Acoustic–gravity waves during solar eclipses: Detection and characterization using wavelet transforms

P. Šauli[a,*], S.G. Roux[b], P. Abry[b], J. Boška[a]

[a]*Institute of Atmospheric Physics ASCR, Czech Republic*
[b]*Laboratoire de Physique (UMR5672), CNRS, Ecole Normale Supérieure, Lyon, France*

Received 31 January 2007; received in revised form 7 June 2007; accepted 23 June 2007
Available online 6 July 2007

This contribution is dedicated to the memory of J. Morlet, one of the fathers of the wavelet transform.

Abstract

In the present contribution, we first propose a methodology that enables to detect wave-like structures propagating in ionosphere, by tracking the local maxima of the modulus of continuous complex wavelet transform coefficients with respect to heights. From the derivation of the phases of the wavelet transform, we measure the corresponding propagation parameters. These tools are applied to measurements collected by vertical ionospheric sounding at high-time resolution sampling regime (sampling periods ranged from 1 to 3 min) in the observatory Průhonice (49.9N, 14.5E, Czech Republic). The aim of these experiments is to analyze the changes in the ionospheric plasma induced by three different solar eclipse events (total solar eclipses, 11 August 1999, 29 March 2006, and annular solar eclipse, 3 October 2005) and to detect and analyze the propagation of the generated acoustic–gravity waves (AGWs). Second, injecting wave vector components measured from the data into the AGW propagation equations, we obtain a full description of the propagation of the waves. This enables us to differentiate AGWs from others wave-like oscillations and to discuss similarities and differences of the waves detected during these three particular events. These procedures also enabled us to detect acoustic waves. We believe that the methodology proposed here brings significant improvement in detecting and characterizing AGW propagations from empirical data and can be readily used in the ionosphere community.

Keywords: Acoustic–gravity wave; Vertical ionospheric sounding; F-layer; Wavelet transform; Wave-packet characterization

1. Introduction

Acoustic–gravity waves in atmosphere: Terrestrial atmosphere shows a high variability over a broad range of periodicities, which mostly consists of wave-like perturbations characterized by various spatial and temporal scales. Amongst atmospheric waves, acoustic–gravity waves (AGWs), whose periodicities range from minutes (pure acoustic waves) to a few hours (upper limit of gravity waves), constitute the source of most of the short-time ionospheric variability. AGWs play an important role in the dynamics and energetics of atmosphere and ionosphere. For instance, they are responsible for momentum and energy transfers from high latitudes to low latitudes and from lower to upper atmosphere. Because AGWs spread energy

*Corresponding author. Tel.: +420 2 7201 6067.
E-mail addresses: pkn@ufa.cas.cz (P. Šauli), Stephane.Roux@ens.lyon.fr (S.G. Roux), Patrice.Abry@ens-lyon.fr (P. Abry), boska@ufa.cas.cz (J. Boška).

1364-6826/$ - see front matter © 2007 Elsevier Ltd. All rights reserved.
doi:10.1016/j.jastp.2007.06.012

between atmospheric regions, they significantly contribute to the global circulation, temperature and compositional structure of mesosphere, thermosphere and ionosphere. AGWs are hence an important component of the atmospheric motion field. AGW propagation also have a significant impact on radio wave propagation conditions. Therefore, analyzing and understanding wave generation mechanisms with respect to specified sources constitute a major goal to improve our knowledge of atmospheric dynamics.

AGW theory (e.g. Hines, 1960) in terrestrial atmosphere has been developed in the sixties and then further extended by various authors (e.g. Hooke, 1968; Hocke and Schlegel, 1996; Fritts, 1989). The first experimental observations refer to AGWs generated by explosive sources and earthquakes (cf. Harkrider, 1964; Row, 1967), and AGWs in Earth atmosphere have been widely studied empirically since. The interests of scientists range from the analysis of the climatology of the gravity waves to case studies of AGW occurrences related to particular events acting as wave sources, such as meteorological systems (see, for instance, Boška and Šauli, 2001; Kelley, 1997; Martinis and Manzano, 1999; Šauli and Boška, 2001), geomagnetic storm (cf. Hocke and Schlegel, 1996; Bruinsma et al., 2006; Hawlitschka, 2006), solar eclipse, etc. Various radio techniques (including ionosonde) were used around the globe to analyze the climatology and case events of AGWs. Numerous measurements and campaigns were conducted aiming at relating the observed gravity waves to their sources (e.g., HIRAC campaign amongst others, cf. Feltens et al., 2001). However, the description, interpretation and understanding of the mechanisms underlying AGW generation and propagation still remain incomplete. This is mostly due to severe difficulties in analyzing real measurements. For instance, it is difficult to decide whether the observed wave characteristics are due to the properties and positions of the AGW sources or to interactions between the propagating waves and the mean flow (convection, tides, planetary waves, etc.), see e.g., Hocke and Schlegel (1996), Fritts and Alexander (2003), Laštovička (2006) or Fritts et al. (2006) for detailed reviews.

AGWs and solar eclipses: During a solar eclipse, atmosphere strongly reacts to the break of ionization flux and heating. At thermospheric heights, the reduction in temperature causes a decrease of pressure over the totality footprint to which the neutral winds respond. Thermal cooling and downward transport of gases lead to neutral composition changes in thermosphere that has significant influence on the resulting electron density distribution. Temperature fluctuations and electron density changes propagate as a wave, away from the totality path, cf. Muller-Wodarg et al. (1998). It has been proposed by Chimonas and Hines (1970) that solar eclipses can act as sources for AGWs. The lunar shadow creates a cool spot in the atmosphere that sweeps at supersonic speed across the Earth. The sharp border between sunlit and eclipsed regions, defined by strong gradients in temperature and ionization flux, moves throughout atmosphere and drives it into a non-equilibrium state. Earth atmosphere shows variable sensitivity to the break of ionization flux. Studies by Fritts and Luo (1993) suggest that perturbations generated by the eclipse induced ozone heating interruption may propagate upwards into the thermosphere–ionosphere system where they have an important influence. At a theoretical level, Kato et al. (1977) demonstrated that, in the atmosphere, gravity waves can easily be radiated in association with almost any motion of the source whilst acoustic waves can be emitted only by supersonic motion. By means of vertical ionospheric sounding, Liu et al. (1998) detected waves excited during solar eclipse event at F1 layer heights and attributed their generation and/or enhancement to changes of temperatures, and variations of the height of the transition level for the loss coefficient and the height of the peak of electron production. Many different mechanisms are likely to contribute to wave generation and enhancement at ionospheric heights. Hence, it is difficult to clearly separate or differentiate each contributing agent and to decide which part of wave field belongs to the in situ generated and which part comes from distant regions. First experimental evidence of the existence of gravity waves in ionosphere during solar eclipse was reported in Walker et al. (1991), where waves with periods of 30–33 min were observed on ionosonde sounding virtual heights. However, inconclusive results of the solar eclipse observations rise from the fact that different solar eclipses produce different plasma motions. Indeed, the travel cone geometry and its angular effects on the magnetized plasmas are different for each eclipse. Studies reported in Farges et al. (2001) suggest a longitudinal diversity of the disturbances with respect to pre-noon and post-noon phases.

Goals of the present contribution: Various experimental studies of the 11 August 1999 solar eclipse (cf. e.g., Farges et al., 2001; Altadill et al., 2001a, b; Šauli et al., 2006a, b) analyzed the relations between AGW generation/enhancement in ionosphere and solar eclipse events. The present contribution aims at enlarging the scope of previously existing studies and at bringing new information about horizontal and vertical propagation characteristics. To do so, AGWs detected during three different solar eclipses (11 August 1999, 3 October 2005 and 29 March 2006) are studied and compared. Description of these eclipses and corresponding data are detailed in Section 2 and Table 1.

Elaborating on tools proposed in Liu et al. (1998), Altadill et al. (2001a) and Šauli et al. (2006a), this contribution also develops a wavelet transform based methodology to detect wave packets (or structures) propagating at ionospheric heights and to measure, from data, their time, period and height locations, their wave vectors, phase and packet velocities. Techniques based on Fourier transforms were previously proposed. However, by definition, Fourier transforms are averaging, and hence mixing information, along time. Therefore, wave parameters measured at a given frequency can potentially result from the contribution of different waves sharing the same characteristic frequency but existing at different time positions, hence producing poor or inaccurate characterization of the waves. Wavelet decompositions, thanks to their being joint time and frequency representations, enable to disentangle the contribution of different structures whose time or frequency supports partially overlap. Therefore, they enable to better identify and analyze wave structures, to more accurately decide whether they consist of AGWs or not and finally to better measure their corresponding propagation parameters.

Table 1
Parameters of the solar eclipse events

Event	First contact	Fourth contact	Maximum	Magnitude
11 August 1999	09:22	12:04	10:42	0.952
3 October 2005	08:01	10:32	09:15	0.539
29 March 2006	09:46	11:50	10:48	0.486

Parameters as observed above Průhonice ionospheric station (according to NASA database, time is given in UT). More information about solar and lunar eclipses can be found on the web page <http://sunearth.gsfc.nasa.gov/eclipse/eclipse.html>.

Further developing this wavelet-based approach, we inject measurements into the equations governing AGW propagation and, making use of an upper atmosphere model (Pietrobon, 2000), we fully characterize the propagating parameters of the detected structures. AGW theory and the upper atmosphere model are described in Section 3. Wavelet decomposition and wave-packet detection and characterization are detailed in Section 4. In Section 5, we discuss the obtained results and conclude.

2. Solar eclipses and data

Solar eclipse events: In the present contribution, we analyze three different solar eclipse events. Two of them, 11 August 1999 and 29 March 2006, represent total solar eclipses, while the third one, 3 October 2005, is an annular solar eclipse. All three solar eclipse events occurred during periods of low geomagnetic activity. Indeed, as shown in Fig. 1, Kp indices remained below or equal a maximum value of 3 (out of 9) for several consecutive days, indicating that ionosphere remained in a quiet state. Therefore, we can consider that measurements reflect the variability due to the occurrence of the solar eclipses. The supersonic motion of the totality/annularity footprint causes shock wave structures in atmosphere, that are further reflected in ionospheric plasma. The parameters describing each solar eclipse are given in Table 1, as observed from Průhonice ionospheric station.

Data measurements and time series: In upper atmosphere, AGWs are observed directly as fluctuations of neutral gas or oscillations of the ionospheric plasma due to the coupling between the neutral and ionized components. Our measurements consist of vertical profiles of electron concentration. For the three eclipses, measurements were performed at the European mid-latitude ionospheric station Průhonice (Czech Republic; 49.9N, 14.6E), using vertical ionospheric sounding techniques. The 1999 solar eclipse was monitored using a classical ionosonde IPS 42 Kel Aerospace and data were collected with a 1-min sampling period. This ionosonde was later (January 2004) replaced by the Digital Portable Sounder 4 (DPS4) hence used for the two latest solar eclipse events. For DPS4 measurements, lower resolution regimes were chosen to enable simultaneous record of ionograms and plasma drift.

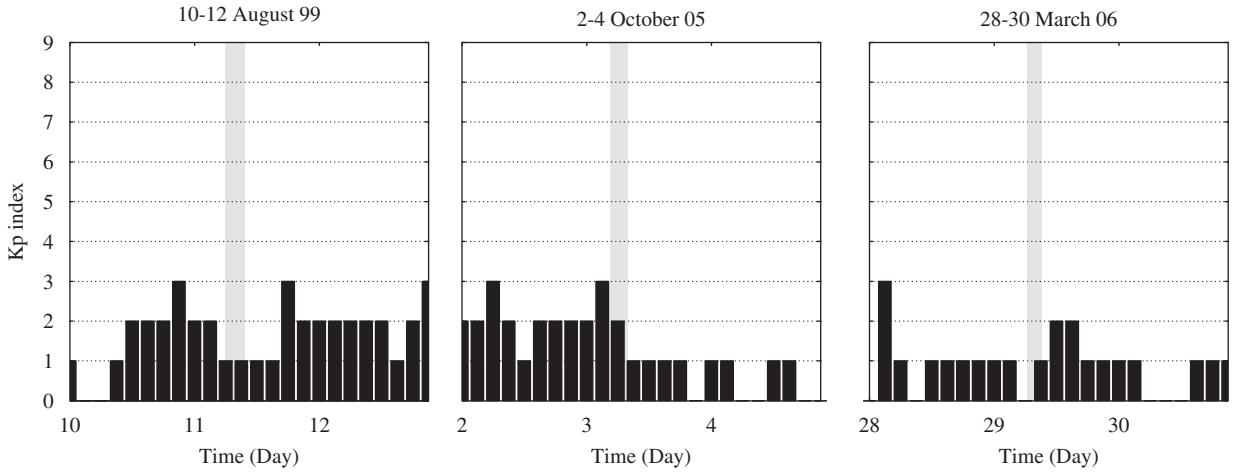

Fig. 1. *Three-hour Kp index*. Geomagnetic activity during three solar eclipses events. The gray shaded areas indicate occurrences time of the eclipses.

Hence data were collected with 2- and 3-min sampling periods for the 2005 and 2006 events, respectively.

Real height vertical electron density profiles were derived from ionograms using two inversion techniques POLynomial ANalysis (Titheridge, 1985) and NHPC (Huang and Reinish, 1996). Finally, from the real height electron density profiles, we obtain variations of the electron concentration X, as a function of time t, at fixed heights z:

$$X(t,z), \quad t \in [T_{\mathrm{m}}, T_{\mathrm{M}}], \ z \in \mathbb{Z}, \tag{1}$$

where T_{m} and T_{M} denote the beginning and end of the measurement in UT. The spatial sampling period is 5 km, corresponding to heights $\mathbb{Z} = \{155, 160, 165, \ldots, 255\}$ (in km). The time series for the three eclipses are shown in Fig. 2, left column. The AGW detection procedures described below are performed on these $X(t,z)$ time series.

3. AGW theory

AGW propagation: At periods of minutes and larger, buoyancy effects become important due to atmospheric stratification and atmosphere becomes dispersive and anisotropic. In such a medium, phase and energy no longer propagate along the same direction. Under an energy conservation assumption, the propagation of AGWs is driven by the following ideal dispersion relation:

$$\omega^4 - \omega^2\omega_{\mathrm{a}}^2 - k_x^2C^2(\omega^2 - \omega_{\mathrm{g}}^2) - C^2\omega^2k_z^2 = 0, \tag{2}$$

where k_x and k_z stand for the horizontal and vertical components of the wave vector, C for the speed of sound, ω_{a} for the angular acoustic cut-off frequency and ω_{g} for the angular buoyancy (or Brunt–Väisälä) frequency. This dispersion relation accounts for a nonlinear and dispersive propagation. It indicates the existence of two propagation frequency ranges: acoustic modes, with characteristic frequencies larger than the acoustic cut-off ω_{a}, gravity modes, with characteristic frequencies smaller than the Brunt–Väisälä ω_{g}. An important property of the gravity mode consists of the fact that energy flows up when phase travels down and vice versa, while for acoustic mode both energy and phase propagate jointly, either upward or downward. The phase propagation angle Φ (measured from the vertical, clockwise) indicates the phase velocity (or wave vector) direction while the energy propagation angle γ (measured from the wave vector direction, clockwise) indicates the packet velocity direction:

$$\tan\Phi = k_x/k_z, \tag{3}$$

$$\tan\gamma = \left(\left(\frac{\omega_{\mathrm{a}}}{\omega}\right)^2 \sin\Phi\cos\Phi\right) \Big/ \left(1 - \left(\frac{\omega_{\mathrm{a}}}{\omega}\right)^2 \sin^2\Phi\right). \tag{4}$$

The modulus of the wave vector, the phase velocity and the vertical and horizontal components of the packet velocity are defined as

$$k = k_x^2 + k_z^2, \tag{5}$$

$$v_\phi = \frac{\omega}{k}, \tag{6}$$

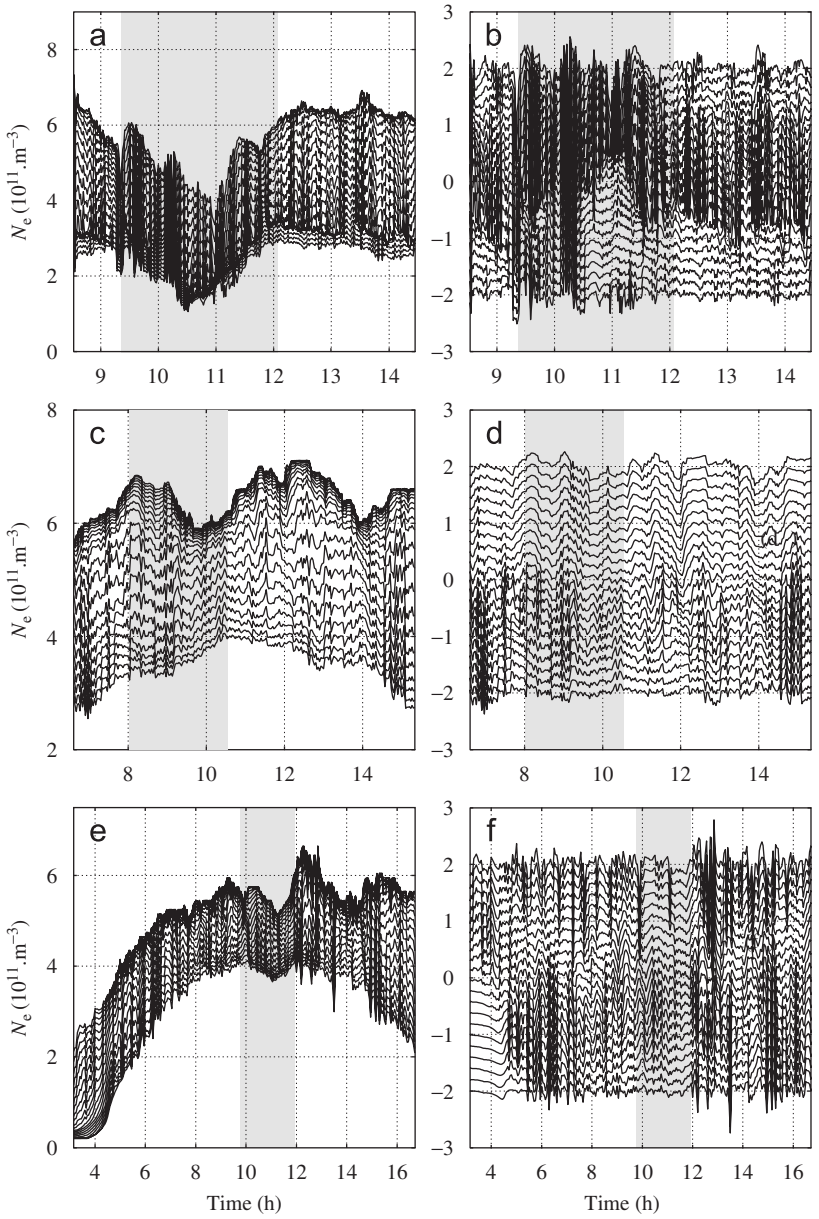

Fig. 2. *Electron concentrations.* Variations of the electron concentrations (at fixed heights 155–255 km) as a function of time for eclipse 11 August 1999 (a) and (b); 3 October 2005 (c) and (d); and 29 March 2006 (e) and (f), (left column) and the corresponding fluctuations left after removing the main trend (right column). For the right column, an arbitrary shift proportional to z is added so that each time series can be seen. The gray shaded areas indicate occurrences time of the eclipses.

$$v_{p,x} = (C^2 k_x(\omega^2 - \omega_g^2))/(\omega(2\omega^2 - \omega_a^2 - C^2k^2)), \quad (7)$$

$$v_{p,z} = (C^2 k_z \omega^2)/(\omega(2\omega^2 - \omega_a^2 - C^2k^2)). \quad (8)$$

Eqs. (2)–(8) are derived in e.g., Hines (1960) or Davies (1990).

Neutral atmosphere parameters: For a practical use of Eqs. (2)–(8), it is necessary to set the values of ω_a, ω_g and C that reflect the properties of the background neutral atmosphere. In our analysis, we consider that the upper atmosphere is well described by the Australian Standard Atmosphere model 2000 (UASA2000). The UASA2000 model is based on U.S. Standard United States Committee on Extension to the Standard Atmosphere (1976) and has been modified in the upper atmosphere, above 86 km (Pietrobon, 2000). The UASA2000 model provides the scale height and acceleration due to

gravity that are necessary to compute the speed of sound. The ratio between the specific heats at constant pressure and constant volume is a key factor in adiabatic processes and in determining the speed of sound in a gas. This ratio takes the value $\gamma = 1.66$ for an ideal mono-atomic gas and $\gamma = 1.4$ for a diatomic gas. Because Earth atmosphere is predominantly a diatomic gas, we use this latter approximation (Davies, 1990; Pröls, 2004).

4. AGW detection and characterization

4.1. Time-scale wave-packet decomposition

The goals of the analyses of the data $X(z,t)$ are to detect the occurrence of coherent wave packets as well as to extract the corresponding wave propagation information. In the literature, this has traditionally been addressed by performing a wave-packet expansion of the data by means of Fourier transform. A methodology, originally introduced in Liu et al. (1998) and Altadill et al. (2001a), proposed to detect waves from the tracking of the maxima of the modulus of the Fourier transforms of the data at different heights z. Propagation parameters were then computed from the corresponding phases of these Fourier transforms. Elaborating on a previous contribution (cf. Šauli et al., 2006a), we extend this original idea to the use of a joint time and frequency representation of the data: the complex valued continuous wavelet transform. Instead of Fourier coefficients, we compute wavelet coefficients, $T_X(w,t,z)$, that account for the information contained in the data $X(t,z)$, at height z, jointly around the time position t and the period $P = 2\pi/w$.

Such time–period coefficients are obtained by comparisons, by means of inner product, of the data $X(t,z)$ against a family of analyzing functions: $T_X(w,t,z) = \langle X(\cdot,z), 1/\sqrt{a}\psi_0((\cdot - t)/a)\rangle$, where ψ_0 is the so-called mother wavelet, a the analysis scale, such that $P = 2\pi a/w_\psi$ (w_ψ is a constant pulsation characterizing ψ_0, cf. Šauli et al., 2006a). For a thorough introduction to wavelet transforms, the reader is referred e.g., to Mallat (1998). In the present work, we adapted the wavelet decomposition Matlab toolbox provided by Torrence and Compo (1998) to our purposes.

The key ingredient of the wavelet analysis lies in the fact that it constitutes a joint time–period representation of the data so that the use, as a mother wavelet, of any oscillating pattern with a satisfactory joint time and frequency localization essentially yields comparable results. In the present contribution, we used the celebrated Morlet mother wavelet and the Paul mother wavelet:

Morlet:

$$\psi_{0,(v_0,\sigma)}(t) = (\pi\sigma^2)^{-1/4} \exp\left(-\frac{t^2}{2\sigma^2}\right) \exp(\imath 2\pi v_0 t). \quad (9)$$

Paul:

$$\psi_{0,N}(t) = \frac{2^N \imath^N N!}{\sqrt{\pi(2N)!}} (1 - \imath t)^{-(N+1)}. \quad (10)$$

Varying the parameters (v_0, σ) and N, respectively, provides a degree of freedom, mostly controlling the number of oscillations of the mother wavelet as well as their time supports that can be easily tuned to a given purpose. For sake of simplicity, in the present text, we mostly conduct all analysis with the Paul 4 mother wavelet, as the corresponding ψ_0 exhibits satisfactory joint time–period resolutions. However, choosing specific mother wavelets ψ_0 could help to better match specific waveforms in the data and hence theoretically improve the wave-packet detection and characterization. For instance, Morlet wavelet (with $2\pi\sigma v_0 = 6$) benefits from a better period localization for large periods, compared to that obtained with Paul 4 wavelet. Instead, the time resolution of Paul 4 wavelet is better. Therefore, a practical rule may be to use Paul wavelet when aiming at detecting structures which are strongly localized in time with low periods, while Morlet wavelet may be preferred for structures with much larger characteristic periods and hence more spread in time. Acoustic waves, with periods of the order of the minutes, are very concentrated in time (cf. De Moortel et al., 2004 for further discussions). Therefore, their detection and characterization are better achieved using mother wavelets with good time resolution. For instance, in Figs. 11 and 12, showing results for an acoustic wave, we choose to use a Paul mother wavelet, with parameter $N = 2$ to further increase the time resolution.

AGW mostly corresponds to waves with periods ranging from a few minutes to an hour. The range of analysis scales a is varied so that the characteristic periods of the wavelets $\psi_a(t)$ covers this entire range.

4.2. Wave-packet detection

The structure detection scheme that we propose is organized in three key major steps:

(1) Data preprocessing and wavelet decomposition.
(2) Energy concentration detection at each altitude and maxima line tracking along altitude.
(3) Wave parameter measurements.

They are detailed below. For explanation purposes, the behavior of the entire detection and characterization procedures is illustrated on a specific example structure, (corresponding to a superb gravity wave) occurring during the 11th August 1999 eclipse (GW1, in Table 2). The corresponding data are shown in Fig. 2 (left plots).

4.2.1. Data preprocessing and wavelet decomposition

For each altitude z independently, a high-pass filter is applied to the time series $\{X(t,z), t \in [T_m, T_M]\}_{z\in\mathbb{Z}}$ to suppress periods larger than 90 min and focus on short term oscillations. Detrended time series are shown in Fig. 2 (right plots). Then, complex wavelet coefficients are computed on these detrended data. Examples of scalograms are presented in Figs. 3 and 10.

4.2.2. Wave-packet detection

First, for the scalograms $|T_X(\omega,t,z))|$, at each z independently, local energy maxima are detected and their time position, period, amplitude and phase recorded. Second, local maxima that exist *jointly* over a *continuous range* of heights z, within a *same time–period neighborhood* are connected together to form *maxima lines*. When different maxima exist in a same time–period neighborhood, the chaining operation is conducted to favor smooth evolutions along z of the local maxima parameters.

Each of these maxima lines correspond to the detection of a wave packet (or wave structure), and consists of the following collection of information:

(1) Altitude range $z \in [\underline{z}, \overline{z}]$ within which the structure is detected.
(2) Precise time position $t_0(z)$ and pulsation $\omega_0(z)$ of the occurrence of the maximum at each height z and the corresponding amplitude $X_0(z) = X(t_0(z), z)$.
(3) Modulus $|T_X(\omega,t,z))|$ and phase $\phi(\omega,t,z)$ of the wavelet coefficients in the time–period neighborhood around the maxima position.

Scalograms, corresponding to different altitudes, showing local maxima marked with ('•') are displayed in Fig. 3(a), (c) and (e). The practitioner can make use of a set of tools for visual inspection of the scalograms and for the manual selection of the structure (or maxima line) he wants to analyze. Then, he can zoom in the scalograms around the time and period locations of the chosen structure. This is illustrated in Fig. 3(b), (d) and (f) for the same altitude. The selected structure is marked by the use of a '▲'.

4.2.3. Wave-packet measurement

From the information collected for each wave packet, we derive the following collection of attributes.

(1) Mean time and pulsation defined as

$$\underline{t_0} = \langle t_0(z)\rangle_z, \quad \underline{\omega_0} = \langle \omega_0(z)\rangle_z, \tag{11}$$

where $\langle\cdot\rangle_z$ means that average is taken over the range of altitude $z \in [\underline{z}, \overline{z}]$.

Table 2
Detected waves

Event	Name	Period (min)	Occurrence	Propagation
11 August 1999	GW1	15, 30	Initial	Upward/downward
	AW1	3–4	Initial	Upward/downward
	GW2	22	After	Upward
3 October 2005	GW1	43	Maximum	Upward
	GW2	20	Recovery	Upward
	GW3	65	After	Upward
	GW4	30	After	Upward
	GW5	32	After	Upward
	GW6	22	After	Upward
29 March 2006	GW1	30	Initial	Upward
	GW2	40	After	Upward

List of the detected and analyzed waves with occurrence period and time (with respect to the eclipse phase). Period of the wave denotes dominant period of the structure.

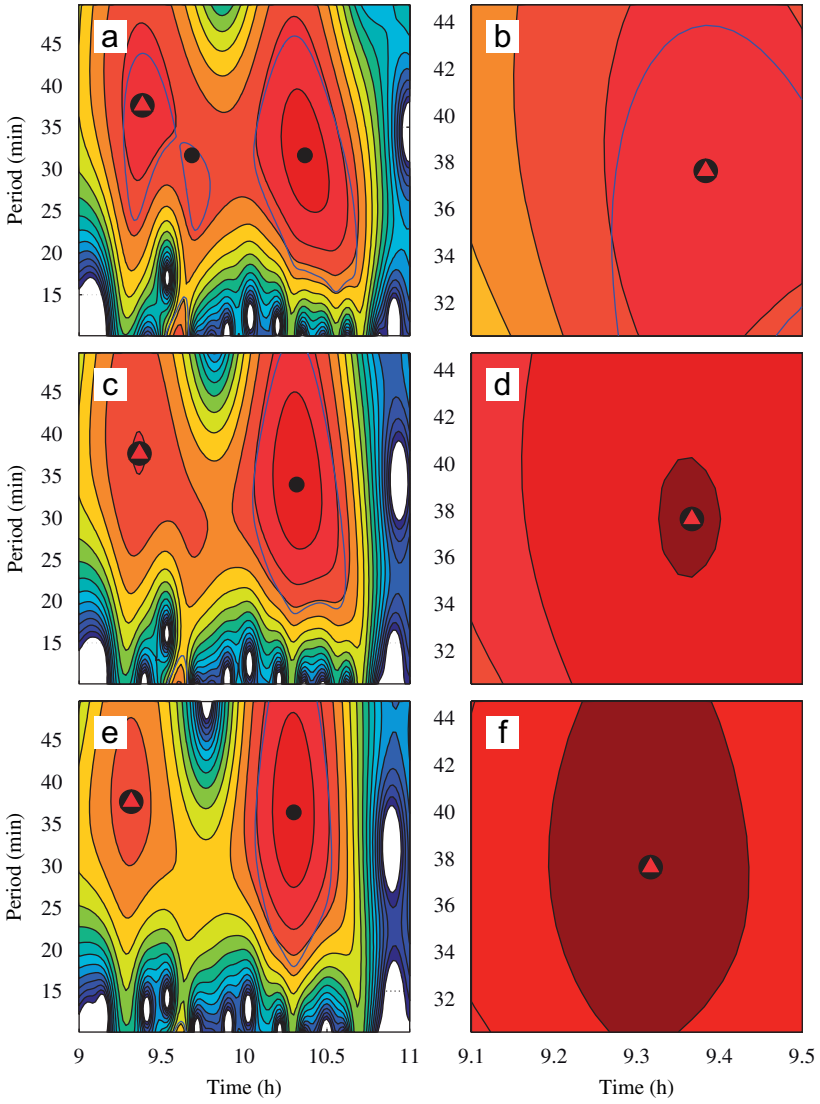

Fig. 3. *Scalograms, 11 August 1999*. Examples of scalogram plots at three consecutive heights 220 km (a) and (b); 215 km (c) and (d); and 210 km (e) and (f). In left column, the time range is selected to cover the initial solar eclipse phase. Local maxima lines are marked with '•'. Around 9 h 15 min UT, there exists a well developed line of local maxima, marked with a '▲', that coincide in time and period over a significant range of heights z. Panels (b), (d) and (f) represent the focus on this maxima in the period range 31–45 min between 9 h UT and 9 h 30 min UT.

(2) Components of the wave vector, phase and packet velocities are measured as

$$\left.\begin{aligned} k_z(\omega,t,z) &= \partial\phi(\omega,t,z)/\partial z,\\ k_{0,z}(z) &= \langle\langle k(\omega,t,z)\rangle\rangle_{t_0(z),\omega_0(z)},\\ v_\phi^{(z)}(\omega,t,z) &= \omega/k_z(\omega,t,z),\\ v_{\phi,0}^{(z)}(z) &= \langle\langle v_\phi^{(z)}(\omega,t,z)\rangle\rangle_{t_0(z),\omega_0(z)},\\ v_{p,z}(\omega,t,z) &= \partial\omega/\partial k_z(\omega,t,z),\\ v_{p,0,z}(z) &= \langle\langle v_{p,z}(\omega,t,z)\rangle\rangle_{t_0(z),\omega_0(z)}, \end{aligned}\right\} \quad (12)$$

where $\langle\langle\cdot\rangle\rangle_{t_0(z),\omega_0(z)}$ denote that we take the median within a narrow time-pulsation neighborhood centered around $t_0(z)$ and $\omega_0(z)$.

Fig. 4 shows $t_0(z)$, $P_0(z)=2\pi/\omega_0(z)$, $k_{0,z}(z)$, $X_0(z)$, $v_{\phi,0}^{(z)}(z)$ and $v_{p,0,z}(z)$ measured according to the procedure described above for the chosen example structure.

This theoretically simple procedure calls for three important practical comments.

Comment 1: Computing the quantities above involves derivation. This is performed using a third-order or fifth-order finite difference procedure, depending on the range of heights available in the structure and border effects are taken care of. Note that the computation of $v_{p,z}(\omega,t,z)$ requires a double derivation and is actually computed as the inverse of $\partial/\partial\omega(\partial\phi(\omega,t,z)/\partial z)$. This is numerically poorly conditioned and may lead to inaccurate results. This is further discussed in Section 6.1 where an acoustic wave is analyzed.

Comment 2: From ionospheric vertical sounding measurements, one only has access to vertical profiles of electron density and hence to the vertical components of the wave vector, phase and packet velocities. Therefore, in Eq. (12) k_z and $v_{p,z}$ stand for the vertical components of the corresponding vectors. For the phase velocity, the situation is even more involved. In Liu et al. (1998), Altadill et al. (2001a) and Šauli et al. (2006a), $v_\phi^{(z)}$ has been incorrectly associated to the z component of the phase velocity $v_{\phi,z}$. However, $v_\phi=\omega/k=\omega/k_z\cdot k_z/k=v_\phi^{(z)}\cos\Phi$, while $v_{\phi,z}=v_\phi\cos\Phi$, hence, $v_{\phi,z}=v_\phi^{(z)}\cos^2\Phi$. When the phase propagation direction is close to the vertical direction, the error is negligible, this is, however, not the case for close to horizontal phase propagation.

Comment 3: The key feature of this procedure consists of the fact that all quantities are computed for each triplet (ω,t,z) independently and a priori. A local averaging (for instance using a median filter) is performed *a posteriori* over a narrow time-pulsation neighborhood for each quantity individually. The alternative choice which would consist of computing Eqs. (12) directly from averaged quantities, such as $k_{0,z}(z)$ would lead to much poorer results.

4.3. Wave-packet characterization

No further information can be extracted from the data themselves. To decide whether a detected wave packet corresponds or not to the propagation of an AGW, it can be compared to the theoretical AGW

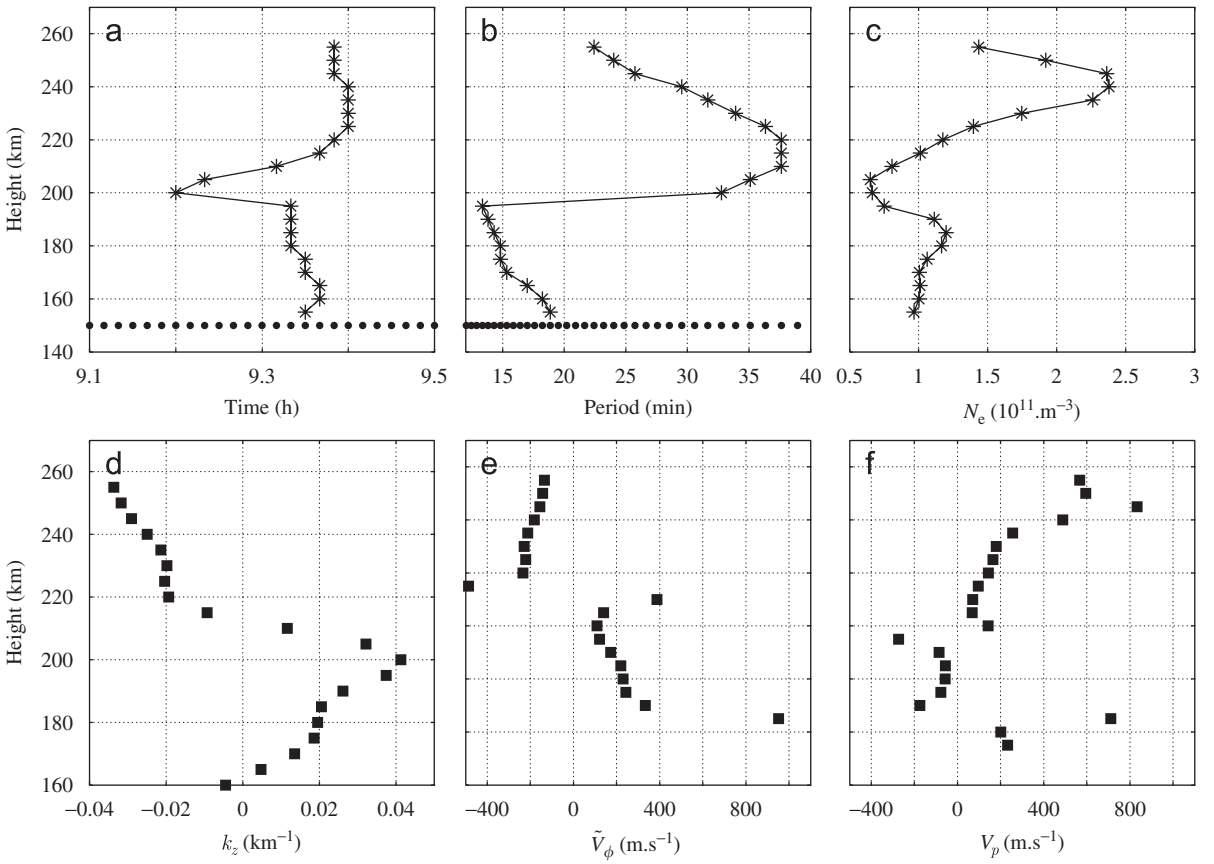

Fig. 4. *11 August 1999*, *GW1*: *detection*. Time location (a), period (b) and amplitude (c) of the detected wave, with the vertical components of the wave vector k_z (d), phase velocity $v_\phi^{(z)}$ (e) and packet velocity $v_{(p,z)}$ (f).

propagation model recalled in Section 3, making use of the upper atmosphere model.

First, from the atmosphere model, we derive the values of $\omega_a(z), \omega_g(z)$ and $C(z)$, for all $z \in [\underline{z}, \overline{z}]$. Comparing the measured $w_0(z)$ to $\omega_a(z)$ and $\omega_g(z)$ enables to check whether the detected structure packet consists of a gravity or acoustic waves.

Second, for all $z \in [\underline{z}, \overline{z}]$ and all t and ω in the time–period neighborhood associated to the studied structure, we derive $k_x(\omega, t, z)$ from the dispersion relation in Eq. (2) by plugging-in the measured $k_z(\omega, t, z)$ and the calculated $\omega_a(z), \omega_g(z)$ and $C(z)$.

Third, making use of Eqs. (3)–(4), we derive the phase and energy propagation angles $\Phi(\omega, t, z)$ and $\alpha(\omega, t, z) = \Phi(\omega, t, z) + \gamma(\omega, t, z)$, respectively, measured clockwise from the vertical direction. Then, we compute the wave vector $k(\omega, t, z)$ and the phase velocity $v_\phi(\omega, t, z)$ from Eqs. (5) to (6). Combining previous results yields the phase velocity components $v_{\phi,z}(\omega, t, z) = v_\phi(\omega, t, z)\cos\Phi(\omega, t, z)$, $v_{\phi,x}(\omega, t, z) = v_\phi(\omega, t, z)\sin\Phi(\omega, t, z)$. To finish with, Eqs. (7)–(8) provide the packet velocity components $v_{p,x}(\omega, t, z)$ and $v_{p,z}(\omega, t, z)$.

Fourth, from these quantities, we compute the median $\langle\langle\cdot\rangle\rangle_{t_0(z),\omega_0(z)}$ (as defined in Section 4.2) for each quantity hence obtaining

$$
\begin{aligned}
&\text{Wave vector}\\
&\quad k_{0,x}(z) = \langle\langle k_x(\omega,t,x)\rangle\rangle_{t_0(z),\omega_0(z)},\\
&\quad k_0(z) = \left\langle\left\langle \sqrt{k_x(\omega,t,x)^2 + k_z(\omega,t,z)^2}\right\rangle\right\rangle_{t_0(z),\omega_0(z)},\\
&\text{Wavelength}\\
&\quad \lambda_0(z) = 2\pi/k_0(z),\\
&\text{Phase angle}\\
&\quad \Phi_0(z) = \langle\langle\Phi(\omega,t,z)\rangle\rangle_{t_0(z),\omega_0(z)},\\
&\text{Energy angle}\\
&\quad \alpha_0(z) = \langle\langle\alpha(\omega,t,z)\rangle\rangle_{t_0(z),\omega_0(z)},\\
&\text{Phase velocity}\\
&\quad v_{\phi,0}(z) = \langle\langle v_\phi(\omega,t,z)\rangle\rangle_{t_0(z),\omega_0(z)},\\
&\quad v_{\phi,0,z}(z) = \langle\langle v_{\phi,z}(\omega,t,z)\rangle\rangle_{t_0(z),\omega_0(z)},\\
&\quad v_{\phi,0,x}(z) = \langle\langle v_{\phi,x}(\omega,t,z)\rangle\rangle_{t_0(z),\omega_0(z)},\\
&\text{Packet velocity}\\
&\quad v_{p,0,z}(z) = \langle\langle v_{p,z}(\omega,t,z)\rangle\rangle_{t_0(z),\omega_0(z)},\\
&\quad v_{p,0,x}(z) = \langle\langle v_{p,z}(\omega,t,x)\rangle\rangle_{t_0(z),\omega_0(z)},\\
&\quad v_{p,0}(z) = \left\langle\left\langle \sqrt{v_{p,x}(\omega,t,z)^2 + v_{p,z}(\omega,t,z)^2}\right\rangle\right\rangle_{t_0(z),\omega_0(z)}.
\end{aligned}
\tag{13}
$$

Again, and as in the detection step, the central point of this characterization step lies in all quantities being computed for each triplet (ω, t, z) independently followed by a local median, performed *a posteriori* over a narrow time-pulsation neighborhood.

Moreover, it is a remarkable fact that all the calculations related to the wave characterization require the use of a single quantity measured from the data: $k_z(\omega, t, z) = \partial\phi(\omega, t, z)/\partial z$ and enables comparisons against other measured quantities such as the z-components of the packet and phase velocities. Fig. 5 shows, for the chosen example structure, the quantities computed according to the procedure described above. Also, it compares the computed $v_{\phi,0,z}(z)/\cos^2\Phi_0(z)$ with the measured $v^{(z)}_{\phi,0}$ as well as the computed and measured z-component of the packet velocities.

4.4. Wavelet-based AGW detection and characterization toolbox

All procedures and programs used to detect and characterize AGW were written and implemented in Matlab, by ourselves. A graphical user interface of this toolbox is implemented for a friendly use and allows an easy selection of the desired structure. This toolbox is fully operational and available upon request.

5. Results and discussions

It is rather uneasy to unambiguously assess causality between the solar eclipse events and the detected wave structures in the ionospheric plasma. Difficulties result from the fact that there are no two exactly identical solar eclipse events and from limitations of sounding techniques. Despite the fact that various AGW sources have been identified, many others remain to be found. Amongst irregular AGW bursts, regular increases of AGW activity were found to occur around sunrise and sunset hours, excited by Solar Terminator movement (cf. e.g., Galushko et al., 1998; Somsikov, 1991; Šauli et al., 2006b). Most of other sources (meteorological systems, geomagnetic and solar disturbances, etc.) and corresponding wave-like oscillations contribute to the irregular patterns of AGW activity observed in the ionospheric plasma. Because the solar eclipses analyzed in the present contribution occur sufficiently after the sunrise hours, we can assume that none of the reported waves are induced by Solar Terminator. During the analyzed sounding campaigns, no wave coming from auroral zone was

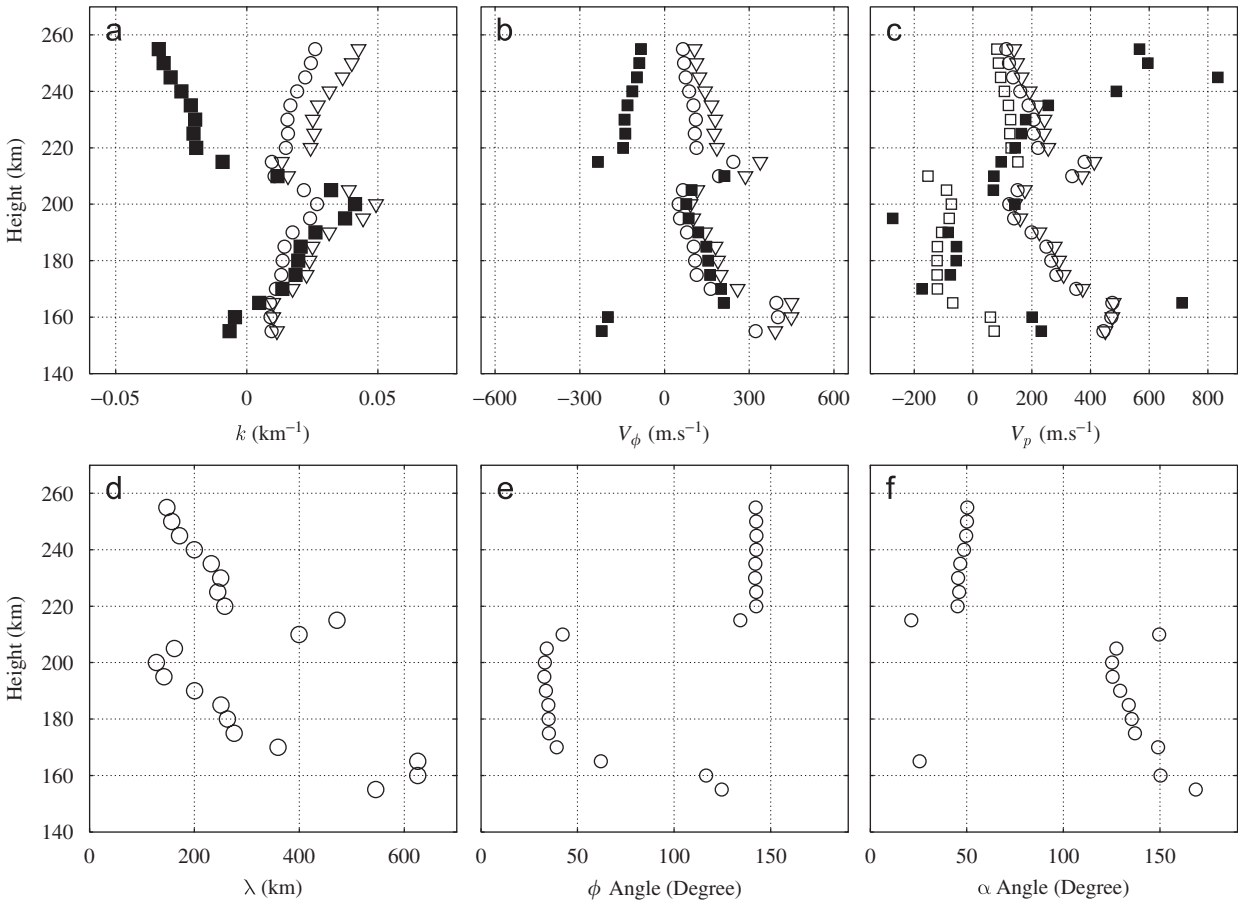

Fig. 5. *11 August 1999*, *GW1*: *characterization.* Wave parameters computed from the AGW theory: wave vector (a), phase velocity (b), packet velocity (c), wave number (d), energy (e) and phase (f) angles. For the vectors of first row, the '□' correspond to the measured (black) and computed (white) z-components, the '○' correspond to the horizontal components while the '▽' are related to the modulus. Note that for the phase velocity (b), the agreement between the measured (black '□') and the computed (white '□') z-component is so satisfactory that the latter can hardly be seen.

expected, due to the quiet geomagnetic and solar activity. Additionally, analysis of meteorological situation above Europe reveals that the Průhonice observatory was in the flank of high pressure ridge. Only rests of dissipating frontal systems were observed. Hence, there is a very low probability of influence, on the ionosphere, of AGW launched from meteorological systems during studied events.

5.1. Wave activity

The three solar eclipses are characterized by an increase of the wave-like oscillation in the acoustic–gravity period range during and after the event. This finding is in agreement with other experimental studies related to observation of the 11 August 1999 event (see, for instance, Altadill et al., 2001a, b; Farges et al., 2003). However, the amplitudes of the oscillations do not remain at the same level during the whole solar eclipse event. Fig. 2(b) shows much larger amplitudes of the fluctuations during the initial phase compared to those occurring after the maximum solar disk occultation. Fig. 2(d) and (f) indicates completely different situations: larger electron concentration oscillation amplitudes are observed after the eclipse maximum and remain present after the fourth contact. Moreover, the two most recent eclipses are characterized by significantly lower magnitudes compared to that of the first one. The decrease of the solar radiation flux is proportional to the magnitude of the eclipse and is

reflected in the depletion of the electron concentrations at all ionospheric heights (compare Fig. 2, left column, plot (a) against (c) and (e)).

After removal of the global decrease/increase, the residual oscillations are analyzed using the wave detection procedures described above. This reveals that numerous wave packets are detected propagating within the ionospheric plasma, before, during and after the solar eclipse events. Most observed waves are characterized by periods ranging from 20 to 70 min and all of them but one consist of gravity waves. All the detected and analyzed waves are listed in Table 2. They are sorted according to their occurrence times (with respect to the phases of the solar eclipse event). Within data, we detected also several waves before the solar eclipse events. We do not report on such waves here since they are very likely not related to the solar eclipse. Due to the fact that all three events occur during morning hours and because the performed measurements cover also sunrise hours, such waves probably originate from Solar Terminator movements. Hence, waves appearing before first contact of each eclipse event are not presented nor further discussed.

5.2. Gravity waves

Let us analyze, for each of the three solar eclipses, the first detected wave, propagating structures within the studied height range.

11 August 1999: Gravity wave 1. This is the wave chosen to illustrate the behaviors of the detection and characterization procedures described in Section 4 and in Fig. 3. Shortly after the first contact around 9 h 20 min UT, an upward propagating structure with period about 30 min and a downward traveling wave with period about 15 min are found. Fig. 4 reports the measurements obtained from the data characterizing these waves. One notices that the downward wave slightly precedes the upward

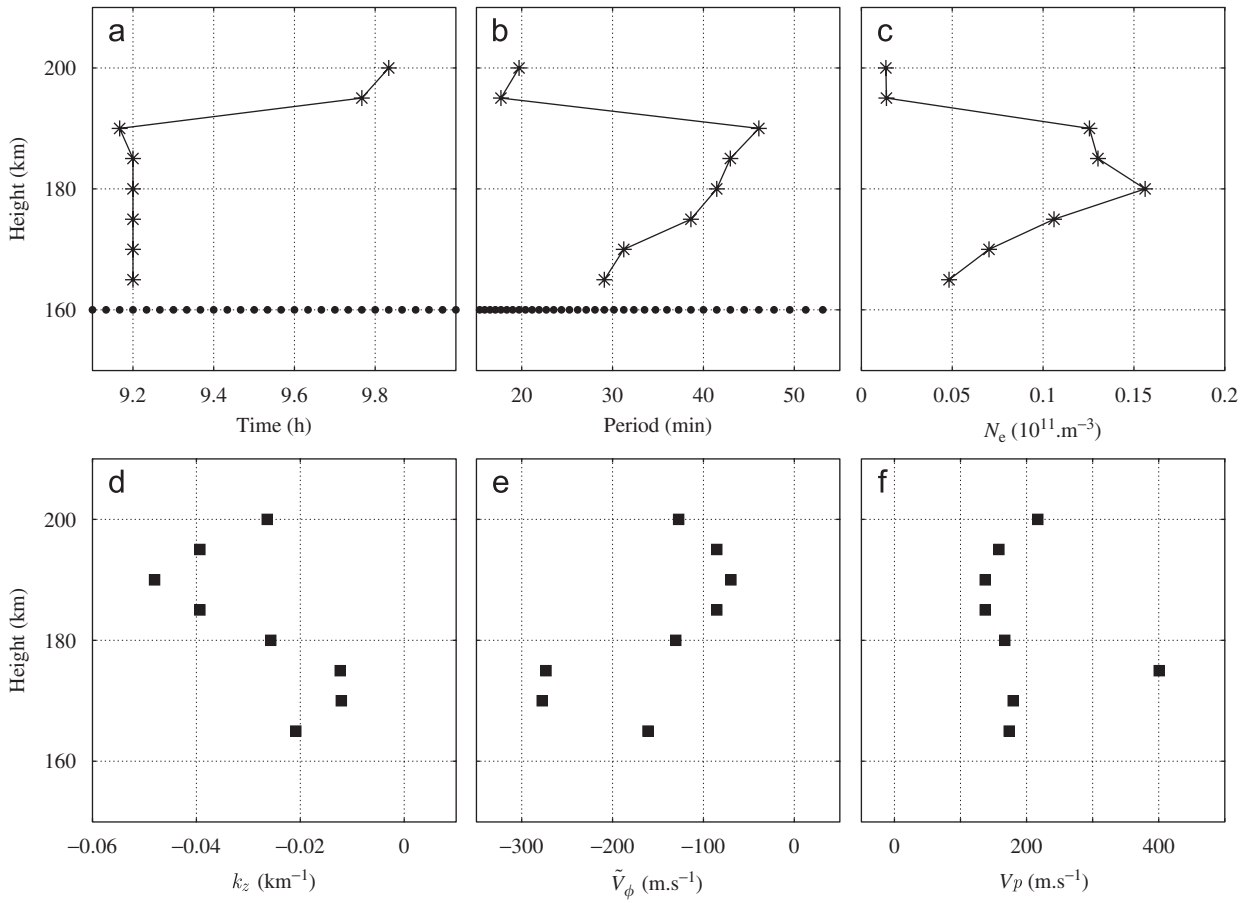

Fig. 6. *3 October 2005, GW1: detection*. Same legend as Fig. 4.

moving wave (Fig. 4(a)). Discontinuity between heights 190 and 210 km in the wave time localization indicates the vertical size of the wave source region. Due to limitations of vertical ionospheric sounding method we cannot precisely decide whether these two waves are emitted from one source or from two distant sources located within region 190–210 km. Parameters of the ionospheric plasma and neutral atmosphere at height 190 km differ from those at height 210 km. Hence, it may influence the resulting upward and downward propagating waves. A discontinuity is also clearly visible in the wave period (cf. Fig. 4(b)), between the periods of the upward and downward moving structures, which indicates that we are observing two independent waves. Maximum amplitude of the upward wave is located around 240 km (see Fig. 4(c)). An important property of gravity waves lies in the fact that the phase propagates downward while the wave is moving upward or vice versa. Fig. 4 shows the wave vectors and the vertical components of the phase and packet velocities measured from the data. The positive sign of the packet velocity, together with the negative sign of the phase velocity, confirms that a gravity wave is found, that propagates upward from altitude 200 km. Conversely, the gravity wave propagates downward below 200 km. Fig. 5 shows all the wave parameters—wave vector, wavelength, phase and packet velocities, phase and energy angles—characterizing the propagations and derived from AGW theory. The validation for the detection of a gravity wave is highlighted by the difference between energy (α) and phase (Φ) angle which is close to 90°. Moreover, one notices that these waves propagates along directions close to the diagonals. Characteristic wavelength is found to be around 200 km.

In this case, as in most cases, we find an extremely satisfactory agreement between the z-components of the phase and packet velocities measured from the data and derived from disperse relation. This agreement takes into account *Comment* 2, made in

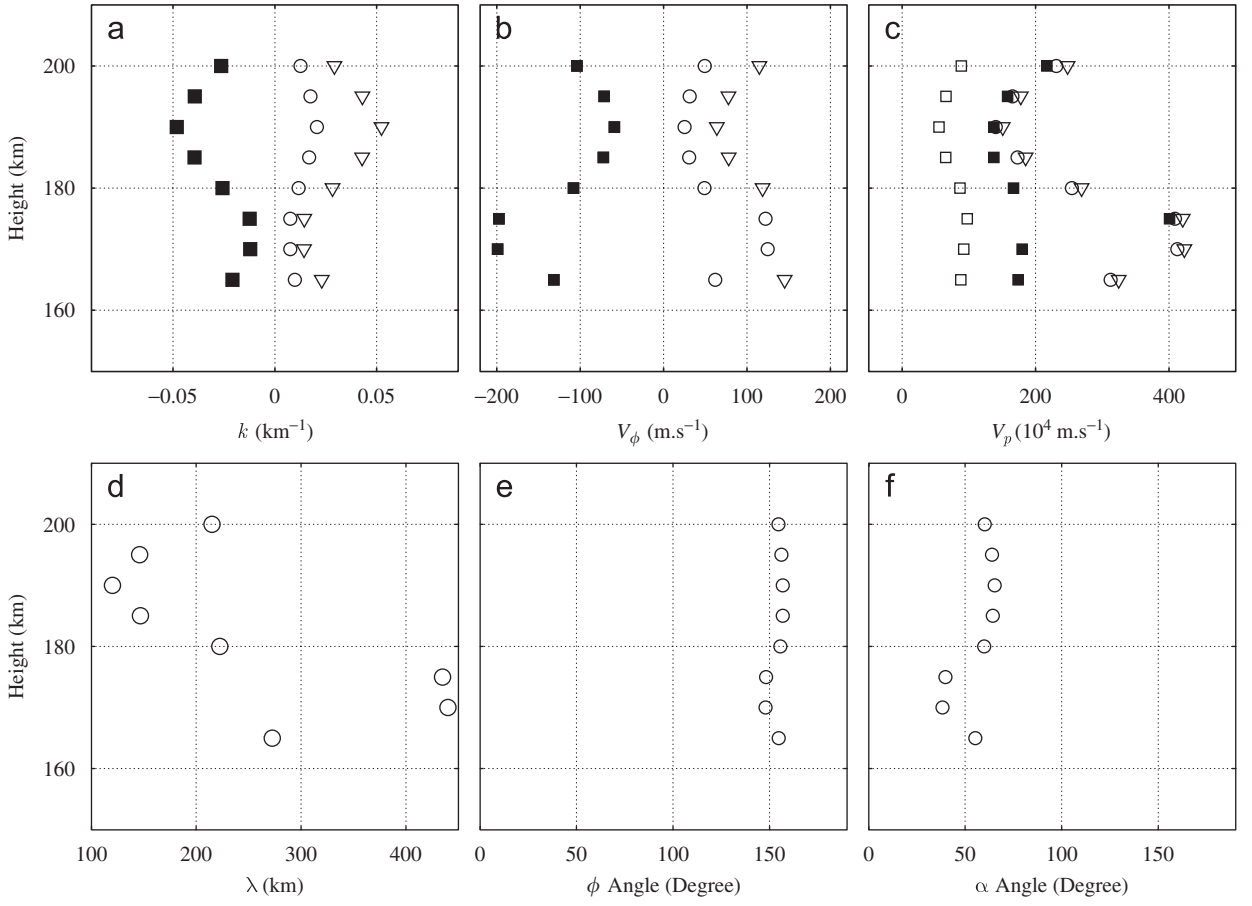

Fig. 7. *3 October 2005*, *GW1*: *characterization.* Same legend as Fig. 5.

Section 4.2 regarding the discrepancy between the measured quantity v_ϕ^z and the z-component of the phase velocity $v_{\phi,z}$. These agreements constitute clear confirmations of the validity of the detection of a gravity wave and a clear validation of the relevance of our combination of measurements made from data and characterization obtained from equations.

3 October 2005: Gravity wave 1. For the 3 October 2005 event, the first detected wave structure occurs at 9 h 12 min, close to the eclipse maximum (see Fig. 6(a)). This gravity wave with period about 40 min (Fig. 6(b)) propagates upward between 155 and 200 km (as seen from the positive packet velocity and negative phase velocities (cf. Fig. 6(e) and (f))). Wave amplitude maximum appears to be at height 180 km. Fig. 7 illustrates the complete propagation characteristics of the gravity wave. Its wavelength is found to be around 200 km (Fig. 7(d)). Comparison of the z-components of the phase and packet velocities (Fig. 7(b) and (c)) shows high agreement between measured values and computed from disperse relation. The fact that wave is propagating obliquely upward with angle α close to 50° indicates that this wave is moving from lower-laying atmosphere. Horizontal component of wave motion suggests that wave originates in distant location, possibly in the region with higher eclipse magnitude. It also explains, why the first gravity wave detected during annular eclipse event is seen as late as close to eclipse maximum.

29 March 2006: Gravity wave 1. For the 29 March 2006, inspection of the wavelet power spectrum indicates that a well developed structure is observed 14 min only after the first contact, cf. Fig. 8(a). This structure propagates through the lower part of the analyzed ionospheric region, from 160 up to 205 km, with a period around 30 min (Fig. 8(b)). Wave reaches its maximum amplitude at height around 200 km (Fig. 8(c)). Fig. 8(d) shows the

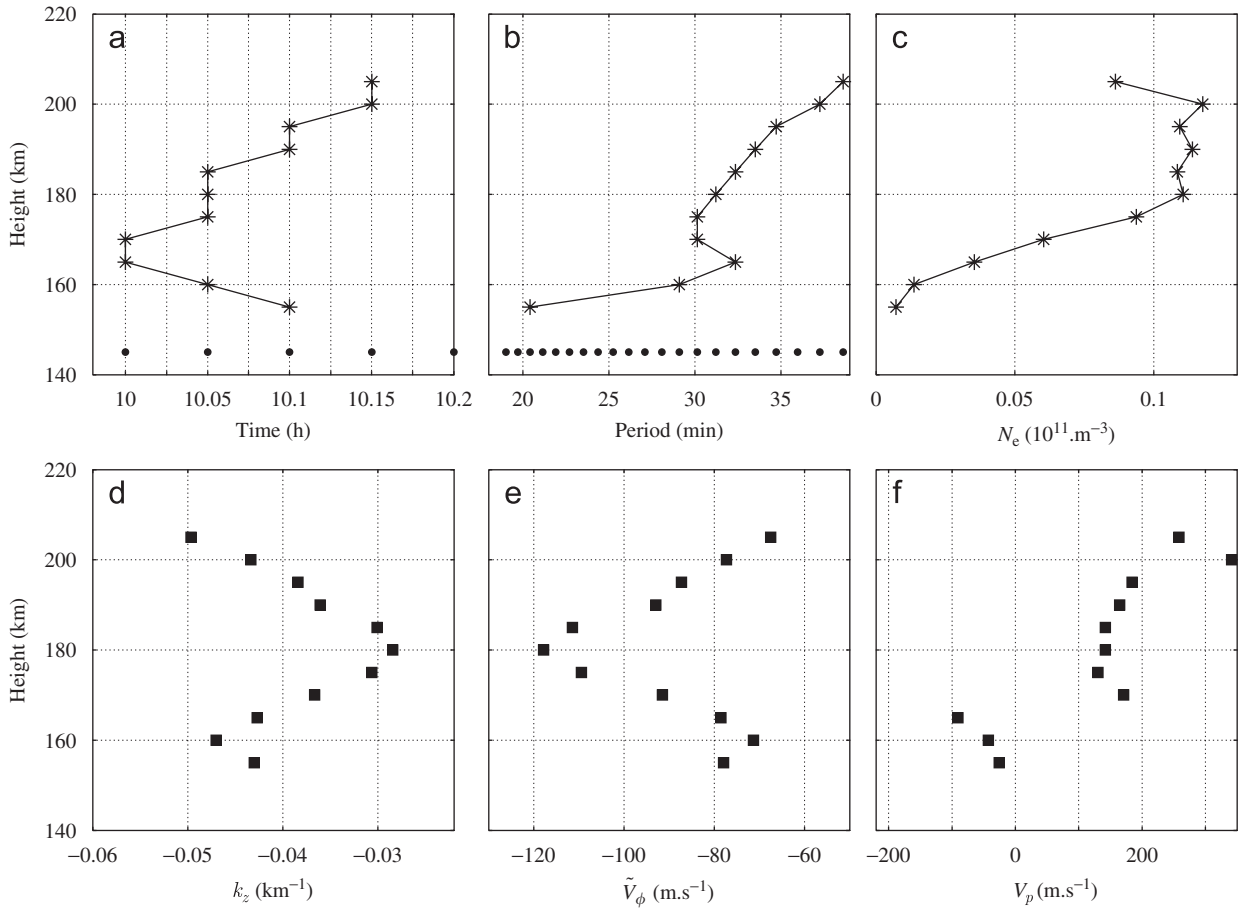

Fig. 8. *29 March 2006, GW1: detection.* Same legend as Fig. 4.

vertical component of the wave vector. The values of the z-components of the phase (negative) and packet (positive) velocities obtained from the data reveal that we observe an upward propagating gravity wave structure (cf. Fig. 8(e) and (f)). The complete set of propagation parameters is illustrated in Fig. 9(a)–(f). Fig. 9(b) shows an excellent agreement between estimated and computed vertical components of the phase velocity. The measured and computed vertical packet velocities do not match perfectly in the whole range (for reasons discussed in Section 4.2), however, there is a reasonable agreement with respect to sign and magnitude. Fig. 9(a) shows the components of wave vector, resulting wavelength λ is plotted in Fig. 9(d). Values of angle α, that characterize energy progression, indicate that detected structure is moving obliquely upward from distant lower-laying source.

6. Discussion

Equivalent analyses and plots for each of the detected structures mentioned in Table 2 are available upon request or can be found at http://www.ufa.cas.cz/html/climaero/sauli.html. The study of these structures yields the following comments.

The gravity wave activity increases after a notably larger delay for the annular solar eclipse compared to the total solar eclipses: waves are found during the maximum phase of the eclipse only for the former while they occur during the initial phase for the latter. This discrepancy in gravity waves generation/occurrence can likely be explained by differences in the terrestrial atmosphere cooling: the border between sunlit and eclipsed region is much sharper in the case of total eclipse.

Analyzing wave propagations, we observe predominantly upward propagating structures. The

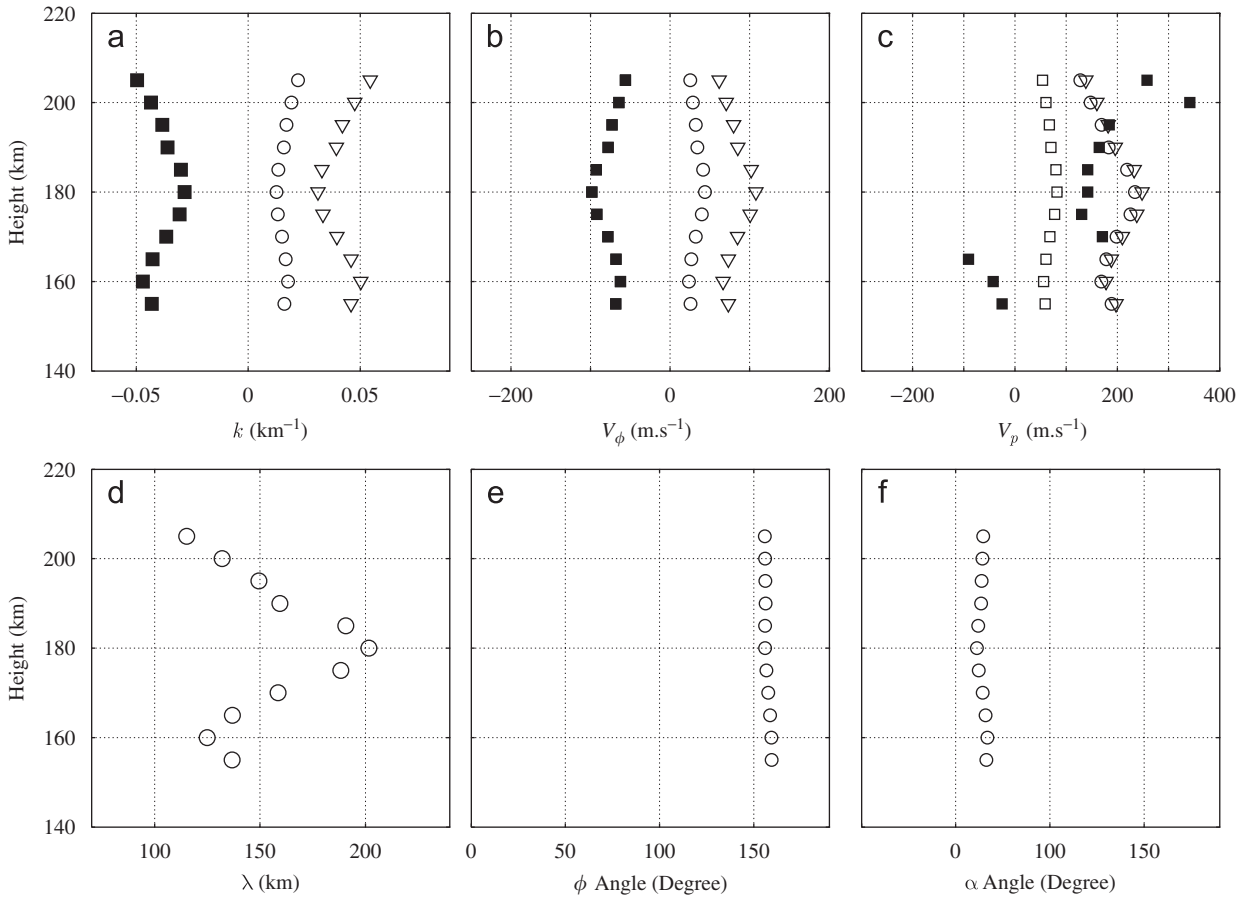

Fig. 9. *29 March 2006, GW1: characterization.* Same legend as Fig. 4.

wave structure that propagate upward and downward from the source region located around 200 km height consists of an exceptional case related to the solar eclipse of 11 August 1999. As it has been proposed by Liu et al. (1998) changes of temperatures, and variations of the height of the transition level for the loss coefficient and the height of the peak of electron production may be effective mechanism for wave generation in situ, at ionospheric heights, during solar eclipse even and such emitted waves may propagate upward and downward from source region. Such a situation does not repeat in any of the two other analyzed events, when the coverage of the solar disk is much lower. This finding might reflect that we mostly observe signatures of the shock wave or structures propagating from further distance during the two later events. Supersonic motion of the moon shadow, that forms shock structure (Chimonas and Hines, 1970; Altadill et al., 2001b) and abrupt of solar radiation with consequent interruption of ozone heating in the lower-laying atmosphere (Fritts and

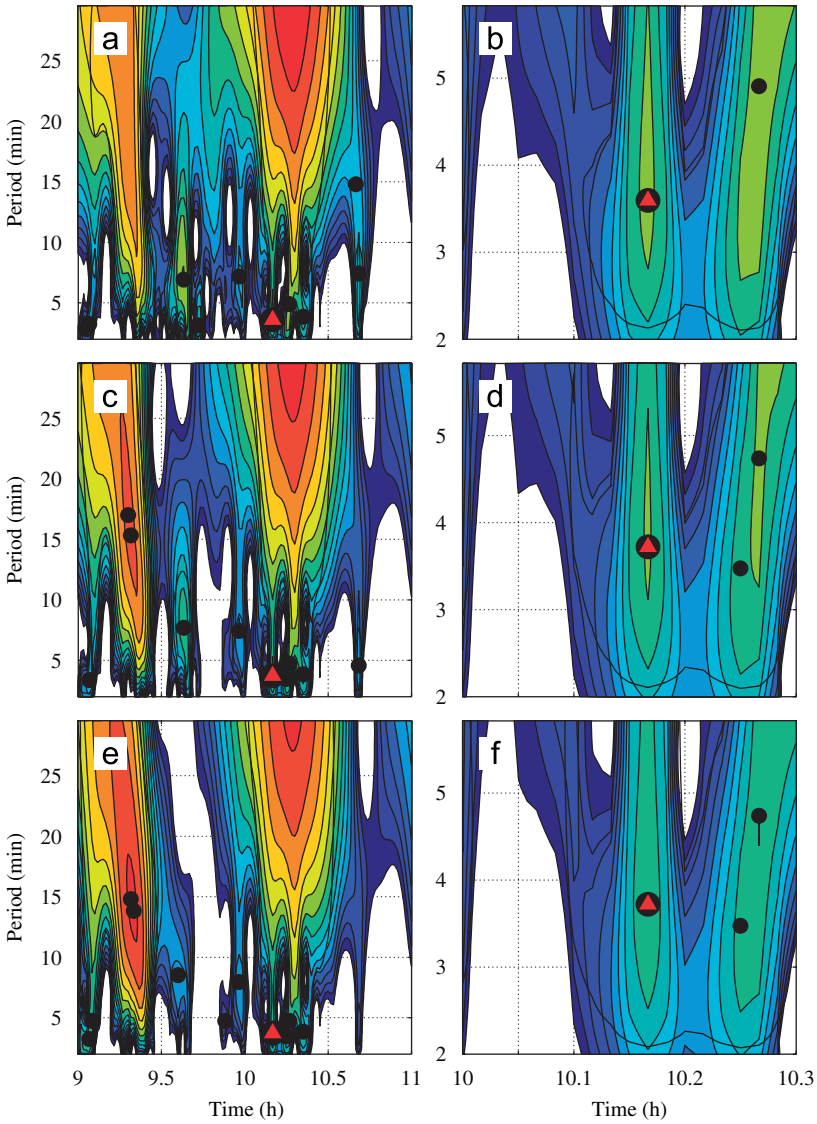

Fig. 10. *Scalograms, 11 August 1999*. Examples of three scalogram plots at three consecutive heights 200 km (a) and (b); 195 km (c) and (d); and 190 km (e) and (f). In left column, the time range is selected to cover the initial solar eclipse phase. Local maxima lines are marked with '•'. Between 10 h UT and 10 h 20 min UT, there is well developed local maxima, marked with a '▲' that coincides in time and period over a significant range of heights z's. Panels (b), (d) and (f) represent the focus on this maxima in the acoustic mode period range 2–6 min around 10 h 15 min UT.

Luo, 1993) may form/launch waves that reach ionospheric heights.

Values of the energy propagation angles α (Figs. 5, 7(f) and 9(f)), of all the detected gravity waves, indicate an oblique propagation direction. The difference between energy (α) and phase (Φ) angles, close to 90°, confirm the gravity wave nature of the detected waves.

6.1. Acoustic wave

During the initial phase of the 11 August 1999 event, we found a line of maxima existing over a large range of heights z and with a period ranging from 3 to 4 min (cf. Fig. 10). The identical signs of packet and phase velocities (cf. Fig. 11), together with the propagation period range suggest that this is an acoustic wave. Fig. 12 shows the characteristics of the wave as derived from the model. For this wave, while the agreement between the measured and derived z-components of the phase velocity is very satisfactory, this is not the case for the packet velocity (cf. Fig. 12(e) and (f)). This can be easily understood as the measured packet velocity involves taking an empirical double derivative, at periods (3–4 min) which are extremely close to the sampling period (1 min): this is hence a ill-conditioned numerical operation. This points out a major difficulty in detecting and characterizing acoustic waves: detecting waves, whose periods are of the order of a few minutes, from data collected at sampling rates commonly used, above 1 min, is barely possible and even meaningless; a relevant tracking of acoustic waves requires the use of sampling periods well below the minute. However, in the 1999 event, the combined use of a wavelet-based time–frequency representation, together with the exceptionally low 1-min sampling period, enables us to unambiguously detect an acoustic wave, which, as far as we know, has very rarely been achieved. Moreover, the use of the equation-based characterization that we proposed here allows us to

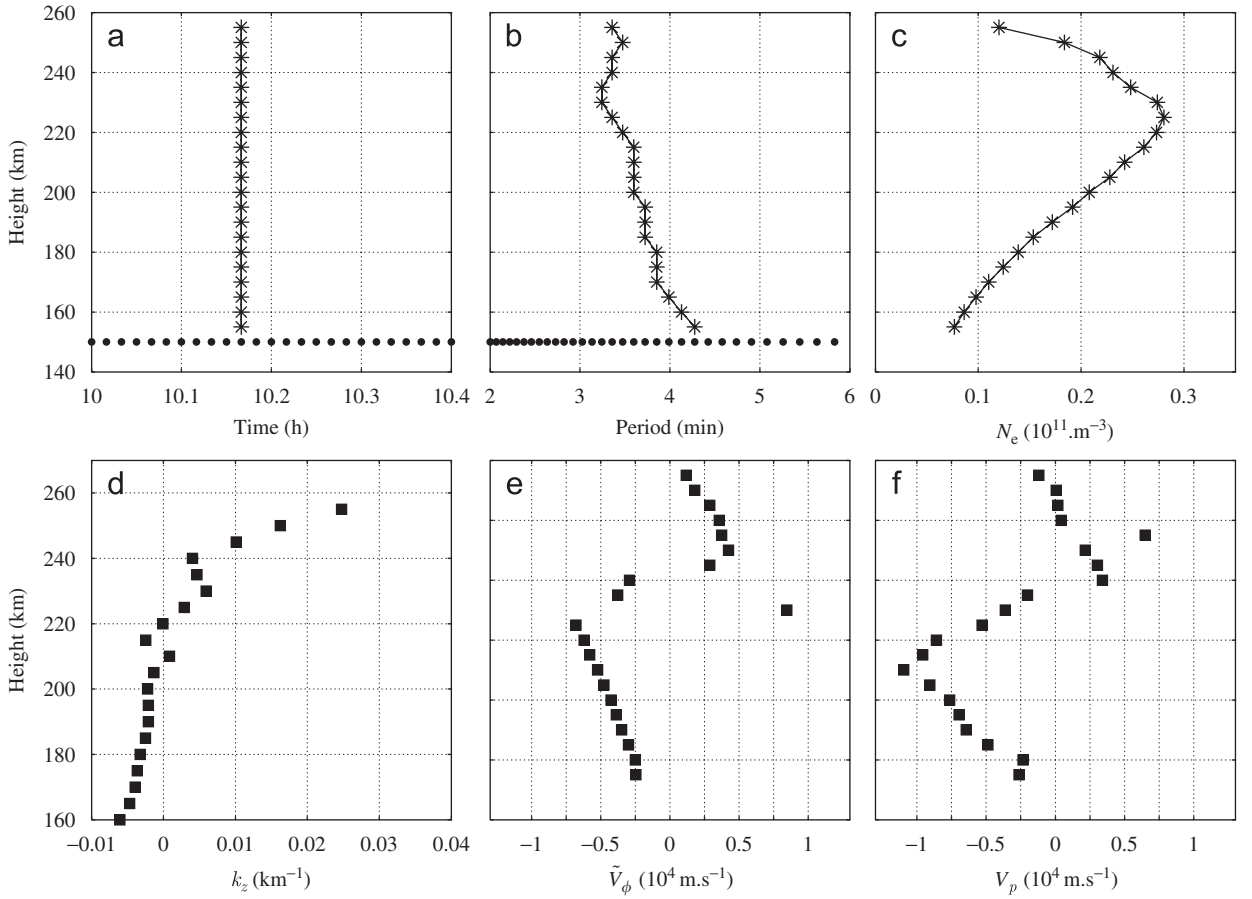

Fig. 11. *11 August 1999, AW1: detection.* Same legend as Fig. 4.

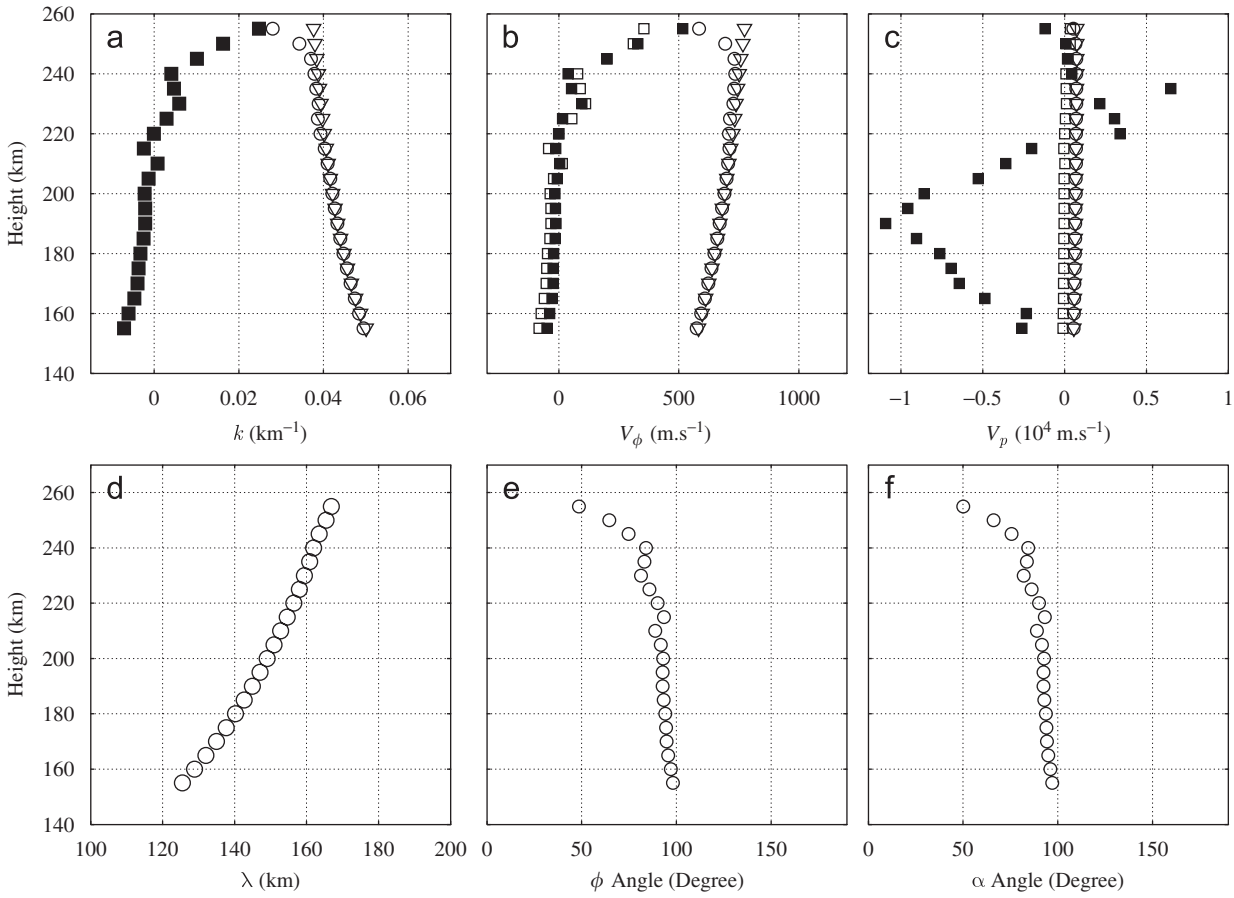

Fig. 12. *11 August 1999, AW1: detection.* Same legend as Fig. 5.

accurately identify its propagating parameters. For instance, we find that the energy and phase angles are close one from the other as opposed to what is found for gravity waves. For this wave, we also find that the value of the energy angle indicate an oblique propagation of the wave. Hence, despite this sampling rate issue, the characterization of the acoustic wave proposed proves valid and gives satisfactory results.

7. Conclusions

In the present contribution, we showed that, taking advantage of the excellent joint time and frequency localization properties of the wavelet transform, we are able to detect and characterize wave structures. The detection relies on the identification of a collection of local modulus maxima, occurring simultaneously over a continuous range of heights. From the (derivation of the) phase of the complex wavelet coefficients, we managed to measure the z-components of the wave, phase and packet velocity vectors. Furthermore, making use of the AGW propagation equations, we managed to fully characterize the corresponding propagating parameters. This characterization part only relies on the use of the measured z-component of the wave vector. A key point in our approach lies in the use of sequences of vertical profiles of electron concentration and in the derivation of vertical and horizontal characteristics of the propagating pulse. Making use of this tools, we were able to identify numerous gravity waves and one acoustic wave. Hence, our analysis confirms the occurrence and production/enhancement of AGWs, at ionospheric heights, during solar eclipses. Notably, we observed that for high magnitude of total solar eclipses AGW occur extremely quickly after the beginning of the event. Also, we highlighted the difficulties in acoustic-wave detection and characterization as well as the need for much higher sampling rate when acoustic waves are targeted.

We believe that the use of the toolbox proposed here brings significant improvements and benefits with respect to efficient wave detections and can hence be easily used by the ionospheric community.

Acknowledgments

This work has been supported by the Grant 205/06/1619 of the Grant Agency of the Czech Republic, Grant IAA300420504 of the Grant Agency ASCR and the joint Grant from French CNRS and Czech ASCR 18098). Authors are grateful to J. Kerum for interpretation of meteorological data.

References

Altadill, D., Sole, J.G., Apostolov, E.M., 2001a. Vertical structure of a gravity wave like oscillation in the ionosphere generated by the solar eclipse of August 11, 1999. Journal of Geophysical Research—Space Physics 106 (A10), 21419–21428.

Altadill, D., Gauthier, F., Vila, P., Sole, J.G., Miro, G., Berranger, R., 2001b. The 11.8.1999 solar eclipse and the ionosphere: a search for distant bow-wave. Journal of Atmospheric and Solar—Terrestrial Physics 63 (9), 925–930.

Boška, J., Šauli, P., 2001. Observations of gravity waves of meteorological origin in the F-region. Physics and Chemistry of the Earth (C) 26 (6), 425–428.

Bruinsma, S., Forbes, J.M., Nerem, R.S., Zhang, X.L., 2006. Thermosphere density response to the 20–21 November 2003 solar and geomagnetic storm from CHAMP and GRACE accelerometer data. Journal of Geophysical Research—Space Physics 111 (A6) Art. No. A06303.

Chimonas, G., Hines, C.O., 1970. Atmospheric gravity waves induced by a solar eclipse. Journal of Geophysical Research 75 (4), 875.

Davies, K., 1990. Ionospheric Radio. Peter Peregrinus Ltd, London, UK.

De Moortel, I., Munday, S.A., Hood, A.W., 2004. Wavelet analysis: the effect of varying basic wavelet parameters. Solar Physics 222, 203–228.

Farges, T., Jodogne, J.C., Bamford, R., Le Roux, Y., Gauthier, F., Vila, P.M., Altadill, D., Sole, J.G., Miro, G., 2001. Disturbances of the western European ionosphere during the total solar eclipse of 11 August 1999 measured by a wide ionosonde and radar network. Journal of Atmospheric and Solar—Terrestrial Physics 63 (9), 915–924.

Farges, T., Le Pichon, A., Blanc, E., Perez, S., Alcoverro, B., 2003. Response of the lower atmosphere and the ionosphere to the eclipse of August 11, 1999. Journal of Atmospheric and Solar—Terrestrial Physics 65 (6), 717–726.

Feltens, J., Jakowski, N., Noll, C., 2001. High-rate solarmax IGS/GPS campaign "HIRAC/SolarMax". CDDIS Bulletin 16 (3).

Fritts, D.C., 1989. A review of gravity wave saturation processes, effects, and variability in the middle atmosphere. Pure and Applied Geophysics 130, 343–371.

Fritts, D.C., Alexander, M.J., 2003. Gravity dynamics and effects in the middle atmosphere. Reviews of Geophysics 41.

Fritts, D.C., Luo, Z., 1993. Gravity wave forcing in the middle atmosphere due to reduced ozone heating during a solar eclipse. Journal of Geophysical Research 98, 3011–3021.

Fritts, D.C., Vadas, S.L., Wan, K., Werne, J.A., 2006. Mean and variable forcing of the middle atmosphere by gravity waves. Journal of Atmospheric and Solar—Terrestrial Physics 68, 247–265.

Galushko, V.G., Paznukhov, V.V., Yampolski, Y.M., Foster, J.C., 1998. Incoherent scatter radar observations of AGW/TID events generated by the solar terminator. Annales Geophysics 16, 821–827.

Harkrider, D.G., 1964. Theoretical + observed acoustic-gravity waves from explosive sources in atmosphere. Journal of Geophysical Research 69 (24), 5295.

Hawlitschka, S., 2006. Travelling ionospheric disturbances (TIDs) and tides observed by a super-resolution HF direction finding system. Journal of Atmospheric and Solar—Terrestrial Physics 68 (3–5), 568–577.

Hines, C.O., 1960. Internal atmospheric gravity waves at ionospheric heights. Canadian Journal of Physics 38, 1441–1481.

Hocke, K., Schlegel, K., 1996. A review of atmospheric gravity waves and traveling ionospheric disturbances: 1982–1995. Annales Geophysicae 14, 917.

Hooke, W.H., 1968. Ionospheric irregularities produced by internal atmospheric gravity waves. Journal of Atmospheric and Solar—Terrestrial Physics 30, 795–823.

Huang, X., Reinish, B.W., 1996. Vertical electron density profiles from the digisonde network. Advances in Space Research 18 (6), 121–129.

Kato, S., Kawakami, T., St. John, D., 1977. Theory of gravity wave emission from moving sources in the upper atmosphere. Journal of Atmospheric and Terrestrial Physics 39, 581–588.

Kelley, M.C., 1997. In situ observations of severe weather-related gravity waves and associated small-scale plasma structures. Journal Geophysical Research—Space Physics 102, 329–335.

Laštovička, J., 2006. Forcing of the ionosphere by waves from below. Journal of Atmospheric and Solar—Terrestrial Physics 68, 479–497.

Liu, J.Y., Hsiao, C.C., Tsai, L.C., Liu, C.H., Kuo, F.S., Lue, H.Y., Huang, C.M., 1998. Vertical phase and group velocities of internal gravity waves derived from ionograms during the solar eclipe of 24 October 1995. Journal of Atmospheric and Solar—Terrestrial Physics 60, 1679–1686.

Mallat, S., 1998. A Wavelet Tour of Signal Processing. Academic Press, San Diego.

Martinis, C.R., Manzano, J.R., 1999. The influence of active meteorological systems on the ionospheric F-region. Annals of Geophysics 42 (1), 1–7.

Muller-Wodarg, I.C.F., Aylward, A.D., Lockwood, M., 1998. Effects of a mid-latitude solar eclipse on the thermosphere and ionosphere—a modeling study. Geophysical Reseach Letters 25 (20), 3787–3790.

Pietrobon, S.S., 2000. Unofficial Australian Standard Atmosphere 2000. ⟨http://www.sworld.com.au/steven/space/atmosphere/⟩.

Pröls, G.W., 2004. Physics of the Earth's Space Environment. An Introduction. Springer, Berlin, Germany.

Row, R.V., 1967. Acoustic-gravity waves in upper atmosphere due to a nuclear and an earthquake. Journal of Geophysical Research 72 (5), 1599.

Šauli, P., Boška, J., 2001. Tropospheric events and possible related gravity wave activity effects on the ionosphere. Journal of Atmospheric and Solar—Terrestrial Physics 63, 945–950.

Šauli, P., Abry, P., Boška, J., Duchayne, L., 2006a. Wavelet characterisation of ionospheric acoustic and gravity waves occuring during the solar eclipse of August 11, 1999. Journal of Atmospheric and Solar—Terrestrial Physics 68, 586–598.

Šauli, P., Abry, P., Altadill, D., Boška, J., 2006b. Detection of the wave-like structures in the F-region electron density: two station measurements. Sudia Geophysica and Geodetica 50, 131–146.

Somsikov, V.M., 1991. Waves in the atmosphere excited by the solar terminator. Geomagnetism and Aeronomy 31 (1) (in Russian).

Titheridge, J.E., 1985. Ionogram analysis with the generalised program POLAN. UAG report-93.

Torrence, C., Compo, G.P., 1998. A practical guide to wavelet analysis. Bulletin of American Meteorological Society 79 (1), 61–78.

U.S. Standard Atmosphere, 1976. United States Committee on Extension to the Standard Atmosphere, 1976. Atmospheric Administration, National Oceanic and National Aeronautics and Space Administration, United States Air Force, Washington, DC.

Walker, G.O., Li, T.Y.Y., Wong, Y.W., Kikuchi, T., Huang, Y.N., 1991. Ionospheric and Geomagnetic effects of the solar eclipse of 18 march 1988 in East-Asia. Journal of Atmospheric and Solar—Terrestrial Physics 53 (1–2), 25–37.